PAPER • OPEN ACCESS

Laminar separation bubble analysis by means of single–shot lifetime temperature sensitive paint in a water towing tank

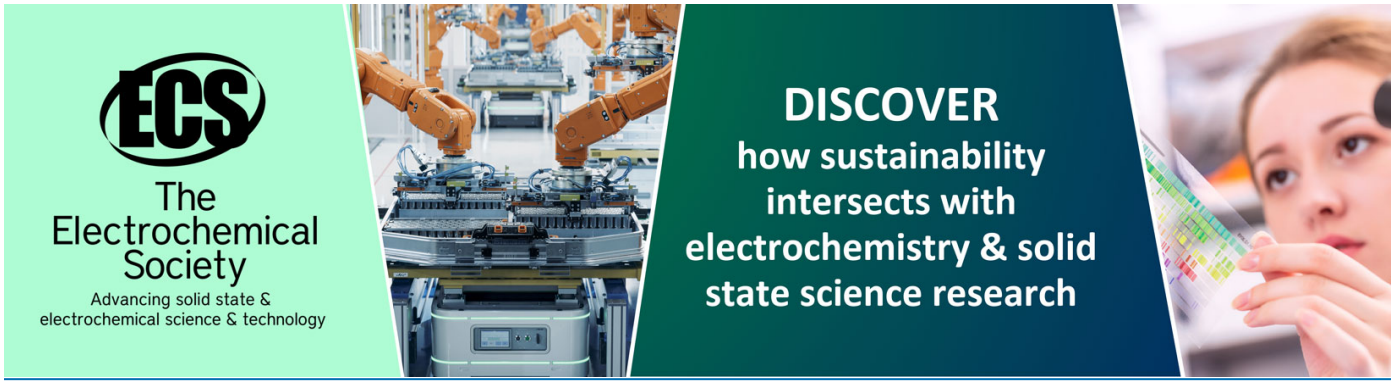

OPEN ACCESS
IOP Publishing
Measurement Science and Technology
Meas. Sci. Technol. **35** (2024) 075301 (13pp)
https://doi.org/10.1088/1361-6501/ad3a85

Laminar separation bubble analysis by means of single–shot lifetime temperature sensitive paint in a water towing tank

Tudor V Venenciuc[1,*], Christian Klein[2], Serhiy Yarusevych[3], Rainer Hain[1] and Christian J Kähler[1]

[1] Institute of Fluid Mechanics and Aerodynamics, University of the Bundeswehr Munich, Werner-Heisenberg-Weg 39, Neubiber 85577, Germany
[2] Institute of Aerodynamics and Flow Technology, German Aerospace Center (DLR), Bunsenstrasse 10, Göttingen 37073, Germany
[3] Department of Mechanical and Mechatronics Engineering, University of Waterloo, N2L 3G1, Waterloo 37073, Canada

E-mail: tudor-victor.venenciuc@unibw.de

Received 24 November 2023, revised 4 March 2024
Accepted for publication 4 April 2024
Published 11 April 2024

Abstract

A laminar separation bubble is studied on an SD7003 foil in a water towing tank at a Reynolds number of $6 \cdot 10^4$ and an angle of attack of 6° by means of the temperature sensitive paint single-shot lifetime method in order to resolve the footprints and dynamics of vortical structures at low inflow turbulence levels. A heat flux is created by applying a carbon based heating layer on the suction side of the foil. The influence of the surface heating on the transition behaviour is analyzed using 2D2C-PIV and found to be negligible. The results demonstrate the capability of the single-shot lifetime method to quantify salient time-averaged flow characteristics, as well as to resolve and characterize the footprints of the dominant coherent structures.

Keywords: laminar separation bubble, temperature sensitive paint, single-shot lifetime, coherent structures

Nomenclature

LED	Light emitting diode
LSB	Laminar separation bubble
PSD	Power spectral density
SNR	Signal noise ratio
TSP	Temperature sensitive paint
c	Chord length
c_f	Skin friction coefficient
c_p	Isobaric specific heat capacity
f	Frequency
g	Gravitational acceleration
h	Heat transfer
I_{GX}	Intensity during gate X
px	Pixel
q_w	Surface Heat flux
Re_c	Chord length based Reynolds number
Ri	Richardson number
St	Stanton number
T	Temperature
T_{free}	Temperature at quiescent conditions
t	Time
t_{norm}	Normalized time units
U_∞	Freestream velocity

* Author to whom any correspondence should be addressed.

$\overline{u'}, \overline{w'}$	Time-averaged streamwise andwall-normal velocity fluctuations
x, y, z	Streamwise, spanwise and wall-normal coordinates
x_S, x_T, x_R	Separation, transition and reattachment streamwise locations
β	Volumetric expansion coefficient
ρ	Density
ν	Kinematic viscosity
τ	Wall shear stress
μ	Dynamic viscosity
σ	Standard deviation
λ	Thermal conductivity

1. Introduction

Small scale aircraft and drones operate at aerodynamically low Reynolds numbers (*Re*) on the order of $\mathcal{O}(\mathrm{Re}) = 10^4 \ldots 10^6$ (Gad-el Hak 2001) and are therefore prone to laminar flow separation. Past separation, the free shear layer typically undergoes transition to turbulence, and the later stages of this process are associated with the formation and shedding of shear layer vortices (Rist 2003, Zhang *et al* 2008). Depending on the *Re*, the angle of attack α and the foil shape, the transitioning separated shear layer may reattach, forming a laminar separation bubble (LSB). Since it plays a prominent role in LSB formation and its inherently unstable behavior, understanding and manipulating the transition process is essential when considering the stability of any small scale aircraft.

Numerous experimental and numerical studies have proven that LSB characteristics depend on the free-stream turbulence intensity and the spectral content of the turbulent fluctuations within the boundary layer prior to separation (e.g. Boyko *et al* 1989, Lang *et al* 2004, Ol *et al* 2005, Burgmann and Schröder 2008, Michelis *et al* 2018, Herbst *et al* 2020). In the experiments of Istvan and Yarusevych (2018), a change in the turbulence intensity from 0.09% to 2.03% significantly altered the time-averaged topology of the LSB. Specifically, the separation location shifted downstream and the height of the bubble reduced due to earlier transition. The behaviour of the separated shear layer is largely governed by the roll-up vortices, which enhance the wall-normal momentum transfer (Kirk and Yarusevych 2017). However, the vortices deform rapidly and break up during the final stages of transition, with the break up process attributed to secondary instabilities, such as elliptical or hyperbolic (Lang *et al* 2004, Marxen *et al* 2013). This is influenced significantly by the disturbance environment in the incoming flow. Higher levels free-stream turbulence intensity have been shown to produce shear layer shedding with lower spanwise coherence and induce earlier vortex break up (e.g. Hosseinverdi and Fasel 2018, Istvan and Yarusevych 2018). Indeed, previous investigations conducted in water tunnel facilities at relatively high free-stream turbulence intensity levels, report the formation of highly deformed coherent structures in the aft portion of the LSB (e.g. Burgmann and Schröder 2008, Hain *et al* 2009 and others). The sensitivity of LSB dynamics to background perturbations motivates the use of water towing tanks with a potential of attaining relatively low free-stream turbulence levels at absolute vortex shedding frequencies one order of magnitude lower than in air flows and at similar *Re* (Yarusevych *et al* 2009). The LSBs observed in these facilities on the same foil have been shown to be comparable to those observed in low disturbance wind tunnels (Ol *et al* 2005).

Experimental investigations of LSBs in typical experimental facilities are complicated by the need to resolve inherently unsteady flow development over a curved foil surface in an elongated, high-shear, near-wall region with a relatively small wall-normal height. This presents significant challenges for all common velocity measurement techniques. An alternative approach may involve a technique that allows interpreting the flow footprint from surface measurements. For example, this has been successfully implemented using the Reynolds analogy between the shear stress and heat transfer coefficient in a number of studies on various geometries, such as flat plates (Liu and Woodiga 2011) and cylinders (Capone *et al* 2015). TSP has been used for this purpose on a curved artificially heated surface (Miozzi *et al* 2019) or cooled incoming flow (Goodman *et al* 2016). The additional surface heating however, may induce natural convection effects. According by Ghiaasiaan (2011), natural convection can only be deemed negligible at a Richardson number (*Ri*) lower than 0.1. Unfortunately, without the additional heating, detecting minute natural thermal perturbations caused by the flow is not feasible at the moment (Costanini *et al* 2021a).

By exploiting the different heat transfer rates of laminar, turbulent, and transitioning flows (Lienhard and Lienhard 2019), it is possible to analyse the time-averaged LSB topology and identify instantaneous footprints of coherent vortical structures. The time-averaged characteristics of the LSB, including the separation (x_S), transition (x_T), and reattachment (x_R) locations can be estimated from the measured surface temperature data and streamwise temperature gradient (e.g, (Spalart and Strelets 2000, Wynnychuk and Yarusevych 2020)). In addition, the onset of thermal fluctuations has been used as an alternative marker for transition location identification (Miozzi *et al* 2019). For the latter method to be viable, however, a working fluid with a sufficiently high Prandtl number is necessary in order to amplify the thermal perturbation amplitude enough so that a camera can capture instantaneous events. In this context, experiments in water facilities, as opposed to wind tunnels, are more conducive to capturing surface temperature fluctuations under an LSB. (Miozzi *et al* 2019) used TSP on a heated model in a water tunnel to estimate instantaneous wall shear stress. However, as discussed earlier, water tunnels typically have relatively high free-stream turbulence intensity (e.g. 0.6% in Miozzi *et al* (2019)).

When considering moving objects, e.g. in towing tanks, the variations in the excitation light patterns must be accounted for, either by using binary paints or the lifetime method. The latter has been employed on moving models to acquire the static pressure (e.g. Mebarki 2016, Weiss *et al* 2017). The data required intense post-processing though and the time-resolved flow features could not be extracted from single snapshots.

The recent advances in the development of luminescent dyes with favourable lifetime properties (Ondrus *et al* 2015), however, have made the lifetime method, formerly known for the low SNR, more viable in environments in which the intensity method cannot be applied. This makes the application of TSP with the lifetime method attractive for towing tank experiments where the foil, cameras, and/or light sources are moved, rendering the basic intensity method infeasible.

This study serves to analyse the feasibility of resolving the near-wall flow features in the aft portion of LSBs by using the temperature sensitive single-shot lifetime method in a towing tank.

2. Experimental Setup

2.1. The towing tank

The experiments are conducted in the open-surface water towing tank of the University of the Bundeswehr Munich. The length, width, and height of the tank are 8 m, 0.9 m, and 0.9 m, respectively. There are four-layered glass sheet windows arranged over 5 m of tank length to provide optical access from the sides and underneath (see figure 1).

The carriage, carrying the foil model and data acquisition instruments, resides on two parallel rails (figure 1). It is driven by a rubber belt run by a servomotor. The system allows for a controlled kinematic sequence, such as constant tow, acceleration and deceleration of varying magnitude, up to a maximum velocity of 1.5 m s^{-1}. The standard deviation of the carriage speed during the tow tests in the present study is 0.56% of the average velocity.

The water temperature is monitored at different locations around the tank using a Testo 108 thermometer with a type T thermocouple attachment. The towing velocity is thus adapted to the changes in viscosity to keep the *Re* constant.

2.2. The foil

An SD7003 foil with a chord length of $c = 250$ mm is chosen for the experiments, since it has been extensively analysed in the literature. It has a total span of 750 mm. The foil was milled after connecting a block of acrylic glass and another of aluminium. The model and some of the geometrical dimensions are displayed in figure 2. The model is equipped with a heating element installed flash into a 0.1 mm groove milled in the suction side (red region in figure 2). First, two copper tape straps are placed at the edges of the groove and led around the leading edge to the pressure side of the foil (figure 3). These are placed flash with the surface in 0.035 mm deep grooves. The copper tapes are connected to electrical wiring on the pressure side. The electrical wires are placed into a spanwise channel machined in the pressure side (see the yellow wires in figure 3) and sealed with silicon. The suction side is covered with easily retractable paper tape, see the right side figure 3, before the wide 0.1 mm deep groove is filled with several layers of Carbo E-Therm (Thermoheld 2022). The product contains electrically conductive carbon nanotubes mixed in a polyurethane base and has been shown to provide low electrical resistance

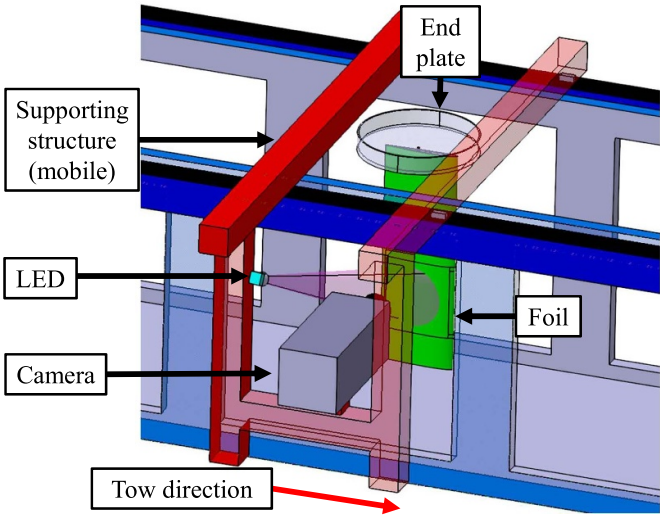

Figure 1. Experimental setup for the TSP experiments. The airfoil (green), support elements (red), end plate (transparent gray), LED, and camera are towed by a carriage at the same velocity. Note that some parts of the tank are omitted or displayed as transparent in order to improve visual clarity.

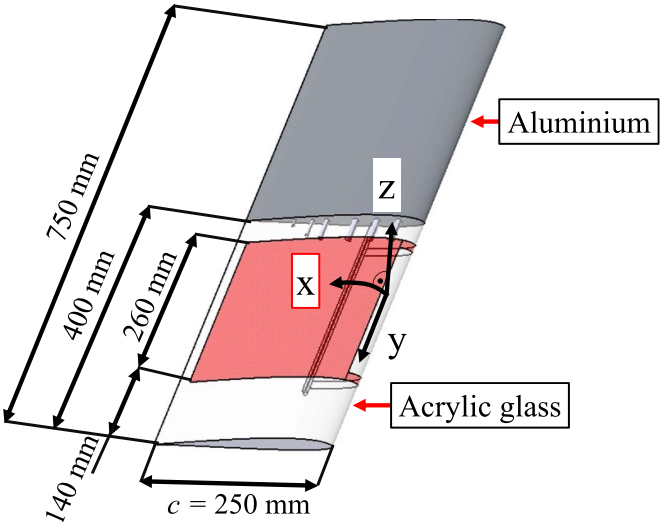

Figure 2. SD7003 model and geometrical dimensions. The red region represents the components of the heating system. The foil is mounted vertically.

(see Klein *et al* 2014 and Goodman *et al* 2016). An 50 µm electrically conductive paint layer was sprayed on the open surface of the foil. The measured electrical resistance is 28.57Ω at a temperature of 20 °C. The entire model is covered with several layers of white paint and then polished with gradually smaller grit sand paper. Finally, the foil is sprayed with TSP on the entire suction side and repolished. The average surface roughness R_a, measured using a Perthometer S2, is 0.042 µm. A QNix 1500 coating thickness gauge is used to measure the TSP layer thickness. Since a metallic underlying layer is necessary for the device, the coating thickness was measured on aluminium calibration coupons, yielding an average thickness of approximately 100 µm.

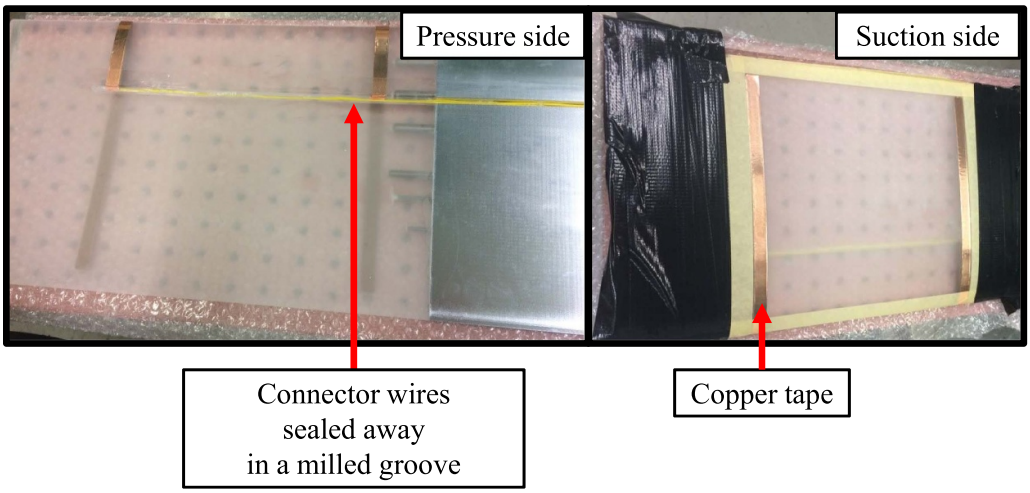

Figure 3. Images of the pressure and suction side of the SD7003 foil during spraying with electrically conductive paint. Left: copper tape being led around the leading edge to the pressure side. Right: suction side which is partially covered with paper and duct tape, before the groove is sprayed with electrically conductive paint.

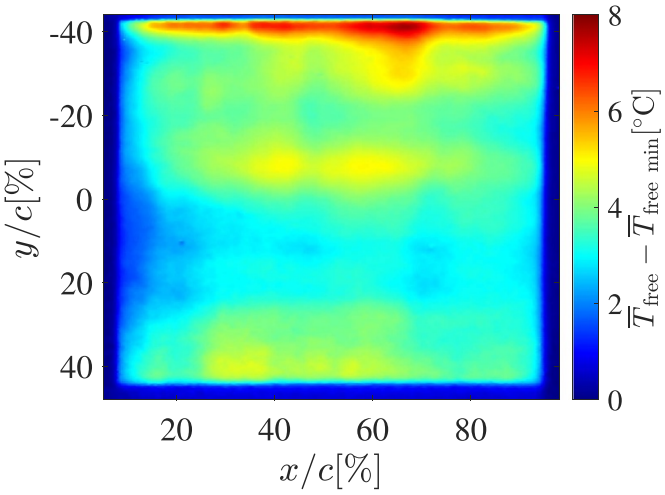

Figure 4. Time-averaged thermal field after a 3 min heat-up in air with the horizontally placed foil at $U_{\text{heat}} = 5$ V.

Figure 4 displays the surface temperature distribution during a heat-up test with the horizontally placed foil in quiescent air. The results show some inhomogeneities in heat flux, but, as will be discussed later, these do not influence the flow transition.

2.3. The experimental setup for the temperature measurement

As displayed in figure 1, the foil is installed vertically in the towing tank. A brush is attached on the lower end of the foil, and upper end is connected to a 400 mm wide and 60 mm tall disk that is adjusted to be partially submerged in order to mitigate end effects.

For the temperature measurement, the suction side is illuminated from the side by 6 UV-LEDs with a peak wavelength of 405 nm from Luminus Devices, Inc.. This conforms to the required excitation spectrum of the TSP employed in the present study. The radiant flux of the LEDs during a 20 ms pulse and a 9 A current is 12.1 W. For a detailed analysis on the properties of the employed luminescent dye, see Ondrus *et al* (2015). The lifetime decay period of the TSP at temperatures similar to those in the present study is 250 µs–300 µs, which is low enough to resolve the expected frequencies. The light sources are operated in pulsed mode by three DK-136 M-1 and three DK-236 drivers. The chosen method of acquiring the surface temperature is the single-shot lifetime method (Liu *et al* 2021). Surface images are acquired in double-frame mode using a Phantom V2640 high-speed camera equipped with a Zeiss Interlock lens with a focal length of 100 mm. The lens is fitted with a 570 nm long-pass interference filter from Laser Components GmbH, type 570ALP 116 410. The acquisition frequency of the camera is chosen to be at least one order of magnitude higher than the expected LSB vortex shedding frequency, which is estimated based on the experiments of Burgmann and Schröder (2008). Table 1 contains additional salient experimental parameters relevant for the temperature acquisition. The TTL signal input for the illumination sources and cameras is provided by a high-speed programmable timing unit PTU X from LaVision controlled with Davis 10.2. The processing and post-processing of the images are conducted with Matlab.

Image preprocessing involves the followings steps. A Savitzky–Golay time filter is applied pixel-wise (Savitzky-Golay Filter 2011) to reduce the influence of the temporal noise of the camera. The Schaefer length M in this case defines the number of entries $(2M+1)$ necessary for the polynomial approximation of a desired order N. A SUSAN blurring filter (Smith and Brady 1997) is employed to reduce the influence of intensity spikes.

The calibration is performed using an aluminium coupon coated with the same luminescent dye as the foil. The coupon is placed on a Peltier device in a calibration chamber filled with air, following the procedure described by Wu *et al* (2017). The

Table 1. Experiment parameters employed for the surface temperature acquisition.

Parameters	Specification
Camera type	Phantom V2640
Acquisition frequency[a] (Hz)	640
Lens focal length (mm)	100
Aperture number	2.8
Sensor resolution (px)	2048 × 1952
Imaging resolution (mm/px)	0.1413
Camera exposure duration (μs)	778
TSP excitation duration (μs)	500
Time filter Schaefer length[b] M	13
Time filter order[b] N	3
Time filter cut-off frequency[b] (Hz)	34.59
Heat flux (W m^{-2})	1764

[a] The camera is operated in double frame mode.
[b] The signal is processed using a Savitzky–Golay time filter, see Savitzky-Golay Filter (2011).

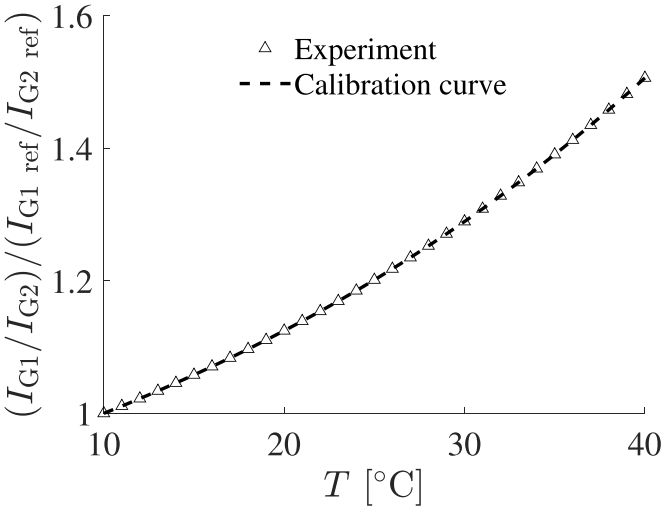

Figure 5. Normalized intensity ratios as a function of the temperature. The value at the lowest temperature of 10 °C is used to normalize all other ratios. The surrounding medium during the calibration was air at approximately 1.013 bar.

exposure and illumination durations are the same as during a tow test. A total of 40 dark and reference (ref) double frames are acquired at temperatures ranging from 10 °C to 40 °C in 1 °C increments. Figure 5 displays the acquired intensity ratios and the calibration function derived from them.

The experimental procedure employed during each tow test is illustrated in figure 6. The 40 dark and ref double images are acquired with the foil aligned at the first window. Afterwards the foil is moved to the back of the tank, where there is no optical access, the heat system is turned on, and after 60 s the tow sequence commences. The wait time is chosen in order to reduce the temperature drift during the test. As soon as the region with optical access is reached, the UV-LEDs and the camera are turned on until deceleration. The camera image timing is adjusted, so that the first image acquires the UV-LED light pulse and the second registers the TSP phosphorescent emission (see figure 6). The averaged dark images are subtracted from the averaged reference and from the images acquired during towing. A marker detection function is used to realign the images acquired during model towing to the reference ones (Bitter and Kähler 2011), but also to monitor the foil vibrations during towing (Bitter *et al* 2012). Figure 7 displays the measured model displacement during a tow test and during a heat-up experiment with the static foil. Since the difference between the spectra is low, it is not expected that the foil deformations influence the experiment.

The surface temperature averaged across the length of the foil between $10\% \leqslant x/c \leqslant 90\%$ and across the span between $-35\% \leqslant y/c \leqslant 40\%$ is displayed in figure 8. For the visualization of the data, the time is normalized with the average tow velocity and the chord length of the foil ($t_{\text{norm}} = t \cdot U_\infty / c$). The time entry $t_{\text{norm}} = 0$ represents the moment when the carriage reaches the region with optical access. By this point, the foil has been towed for at least 10 convective time units and based on the PIV data of Dierl *et al* (2023) in the same facility and at similar flow parameters, the bubble has already reached a quasi-steady state. A stable thermal field could be achieved only after the carriage reaches the third window, therefore after approximately 7 convective time units after the initiation of the image acquisition, which is considered when averaging the data.

The Richardson number quantifies the effect of natural to forced convection in a boundary layer. It is computed as:

$$Ri = \frac{g\beta\,(T_{\text{surface}} - T_\infty)\,c}{U_\infty^2} \tag{1}$$

with the gravitational acceleration g and the volumetric expansion coefficient β. The heating power is adjusted to maintain an as low as possible Ri while still resolving salient flow features of interest. At a water temperature of 19.8 °C and $Re_c = 6 \cdot 10^4$, a surface temperature increase of 8 °C would correspond to $Ri \approx 0.1$. The effects of the natural convection on the flow is therefore considered in the analysis of the results.

2.4. The experimental setup for the PIV measurements

Velocity measurements are conducted on suction side of the foil in order to provide a baseline flow evaluation and to assess the influence of the natural convection on the transitional flow. Two LaVision Imager CX-16 cameras are attached to the carriage as depicted in figure 9. A Photonics DM150-532 DH Nd:YAG double pulse laser illuminates a wall-normal plane as the model is towed across the length of the tank. Runs are performed with the heating system turned on and off, with 10 runs performed for each of the two conditions. The flow was seeded with 10 μm hollow glass spheres. The salient parameters relevant to PIV measurements are listed in table 2.

A multi-pass cross-correlation algorithm is applied with an initial window size of 256 × 256 pixels (px) and an overlap of 50% and a final window size of 32 × 32 pixels with an overlap of 75%. Outlier detection employing a median filter with 5 × 5 kernel and a median absolute deviation threshold of 2 standard deviations is applied to the velocity field (Raffel *et al* 2018).

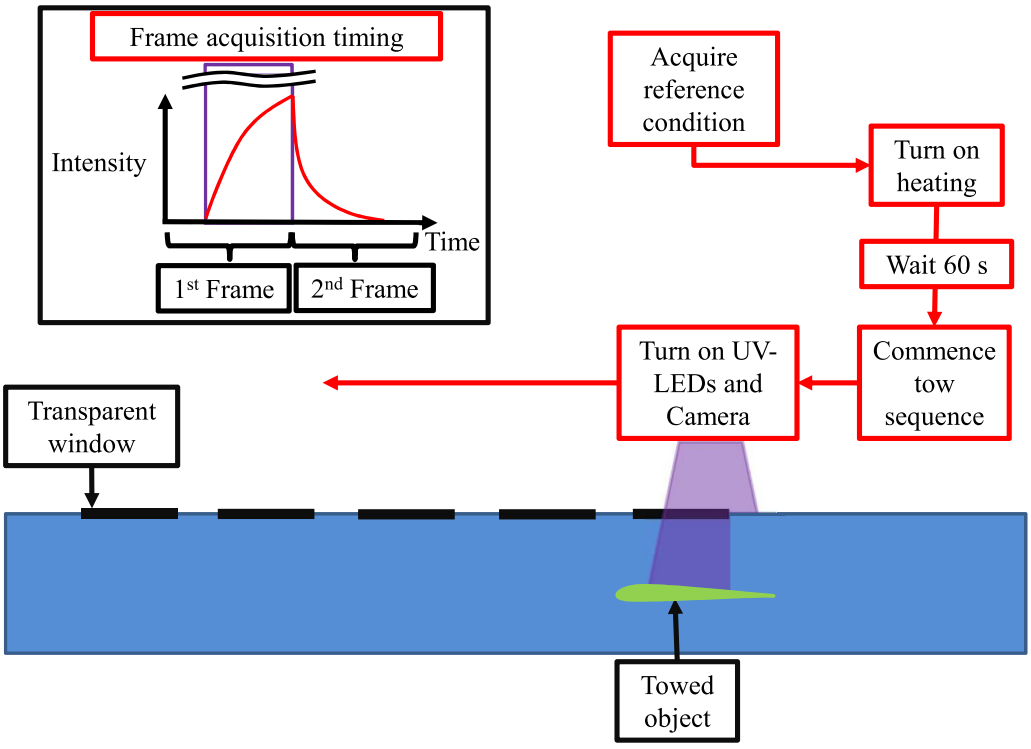

Figure 6. Schematic of the data acquisition process during a tow experiment (top view).

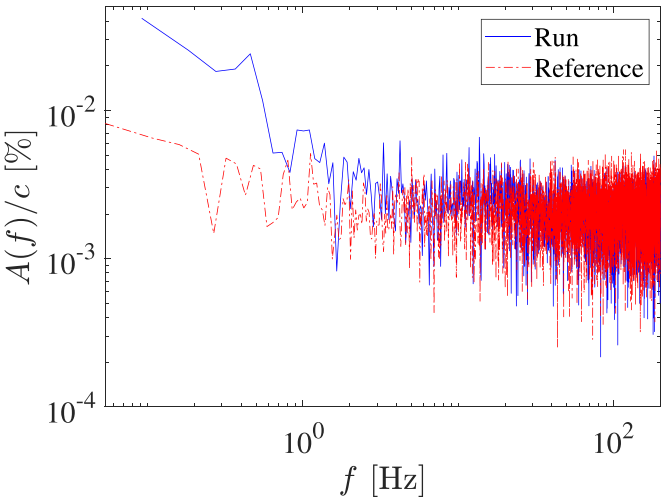

Figure 7. Marker center displacement ($\sqrt{x'_{\text{center}}2 + y'_{\text{center}}2}$) acquired during the tow and during a static heat-up test at 640 Hz. The amplitude is normalized with the chord length.

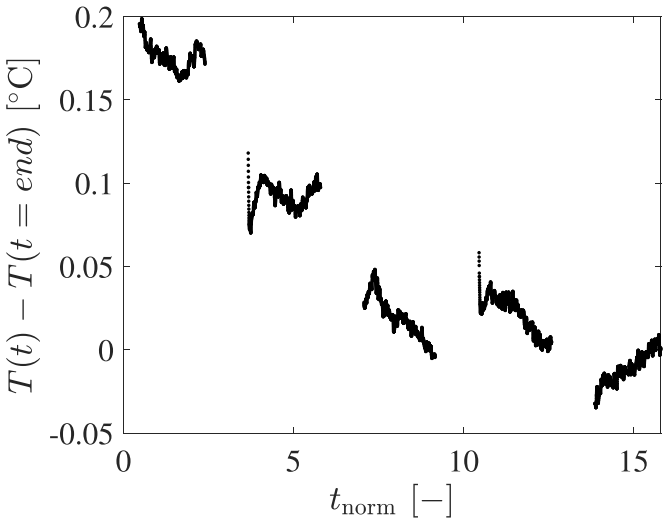

Figure 8. Spanwise and streamwise averaged temperature progression over time.

3. Results

3.1. Effect of the surface heating on the LSB

The Reynolds shear stress ($\overline{u'w'}/U_\infty^2$) fields with the heating system turned on and off at the same intensity as during the TSP tests are displayed in figure 10. The overlaid streamlines (dashed lines) show a displacement topology characteristic of an LSB. Comparing the results, it can be seen that the onset of substantial velocity fluctuations occurs at approximately the same chordwise location with and without surface heating. The maximum Reynolds shear stress along the wall-normal direction shown in figure 11 confirms a close agreement between the results with and without surface heating. Thus, it can be concluded that surface heating employed in the present investigation has negligible effect on the transition

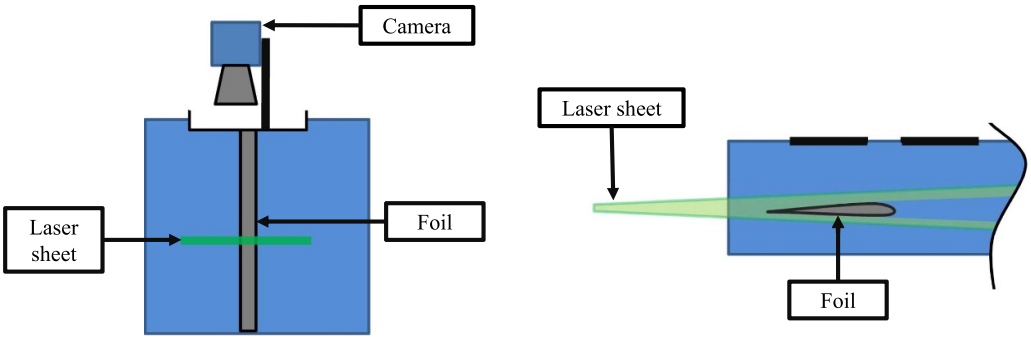

Figure 9. Schematic of the instrument positioning during the PIV data acquisition. Left: frontal view. Right: view from above.

Table 2. Experiment parameters employed for the PIV measurements.

Parameters	Specification
Cameras	2 × LaVision Imager CX-16
Acquisition frequency (Hz)[a]	40.7
Image pairs acquired	1668
Lens focal length (mm)	100
Aperture number	2.8
Sensor resolution[b] (px)	5312 × 1350
Free stream particle image Displacement (px)	17
Imaging resolution (mm/px)	0.0161
Final window size (px)	32 × 32
Vector pitch (mm)	0.129
Laser pulse delay (ms)	1
Particle specific gravity[c]	1.1

[a] The cameras are operated in double frame mode.
[b] This applies to both cameras.
[c] The tracer particles are 10 μm hollow glass spheres.

process in the LSB. It should be note that, due to the high velocity gradients and the diffusely reflective surface, the near-wall velocity in the LSB could not be measured reliably, inhibiting the estimation of mean separation, transition, and reattachment locations based on boundary layer parameters. However, the separation location was determined based on the examination of particle images as the first location where the seeding particles near the wall become nearly static (Nati *et al* 2015). The estimated separation location for the heated case is $x/c = 16.1 \pm 1.36\%$ and for the unheated case $x/c = 15.2 \pm 1.33\%$.

3.2. The mean LSB location derived from TSP data

In this section, the extraction of the relevant mean LSB characteristics from the results of the TSP measurement is presented. The analysis is similar to the Reynolds analogy between the wall shear stress and heat transfer coefficient explored in a number of previous studies (e.g. Duan and He 2014, Abramov and Butkovskii 2021, Kuwata 2021). For a subsonic air flow with a Prandtl ($Pr = c_p\mu/\lambda$) number of $Pr \approx 1$ and with absent pressure gradients (Schlichting and Gersten 2017), the Reynolds analogy can be expressed as:

$$\frac{c_f}{2} = St \tag{2}$$

with the skin friction coefficient $c_f = \tau_w/0.5\rho\ U_\infty^2$ and the Stanton number $St = h/\rho c_p U_\infty^2$. While the determination of skin friction for different fluids on complex geometries is an ongoing topic of research (e.g. Miozzi *et al* 2016, 2019, Costanini *et al* 2021b), here, based on wall temperature and heat flux estimation, we explore simplified relations between the dependant variables, namely, shear stress, heat flux, and temperature distribution at the wall, to identify salient features in near-wall flow development. The associated analysis presented below explores the approaches proposed in several previous studies (Miozzi *et al* 2019, von Hoesslin *et al* 2019, Wynnychuk and Yarusevych 2020, Guerra *et al* 2023).

The time-averaged thermal field is displayed in figure 12. A region with elevated levels of temperature is observed between approximately $20\% \leqslant x/c \leqslant 35\%$, which is caused by the low levels of convective heat transfer at separation and over the fore half of the bubble (Spalart and Strelets 2000). As the transition progresses in the shear layer, the associated velocity fluctuations lead to an increase in heat transfer rate and thus lower surface temperature in the aft portion of the LSB. The highest heat transfer rate downstream of separation occurs at the time-averaged reattachment location (von Hoesslin *et al* 2019). Note, the abrupt decrease of surface temperature at approximately $x/c \approx 40\%$ across the span of the heating element indicates the reattachment behaviour is not greatly influenced by the surface heat flux inhomogeneity.

Figure 13 displays the standard deviation of the thermal signal. A notable increase in fluctuation magnitude can be observed at $x/c \approx 35\%$, which shows that transition exhibits a high degree of uniformity across the span. Note that the spikes visible at the upper edge of the heating layer are caused by reflections of the LEDs in the tank windows. These, however, do not obscure the heated region. The additional dots visible at for example $x/c = 73\%$ and $y/c = 15\%$ are caused by the low intensity signal at the surface marker positions.

Extracting x_S, x_T, and x_R from the temperature distribution and its gradient alone has been shown to provide accurate

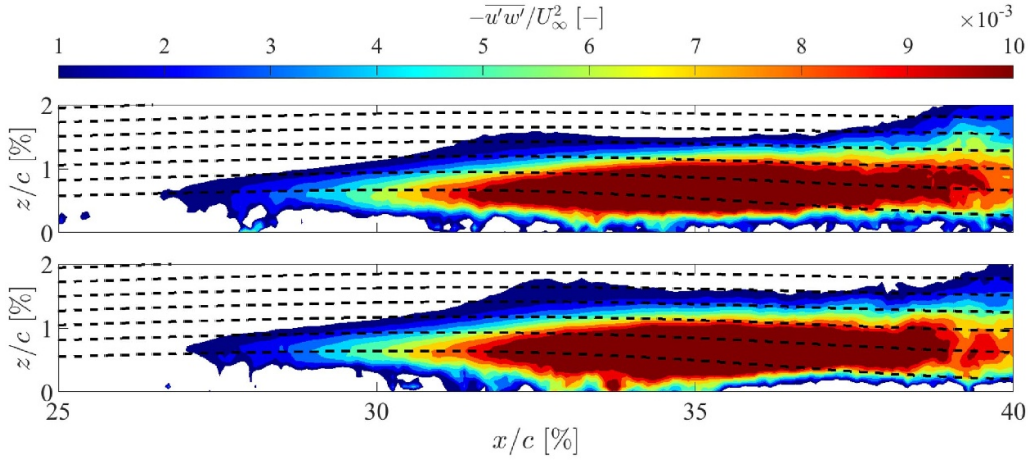

Figure 10. Reynolds shear stress for the heated (up) and non-heated case (down) overlapped with streamlines (dark dashed lines).

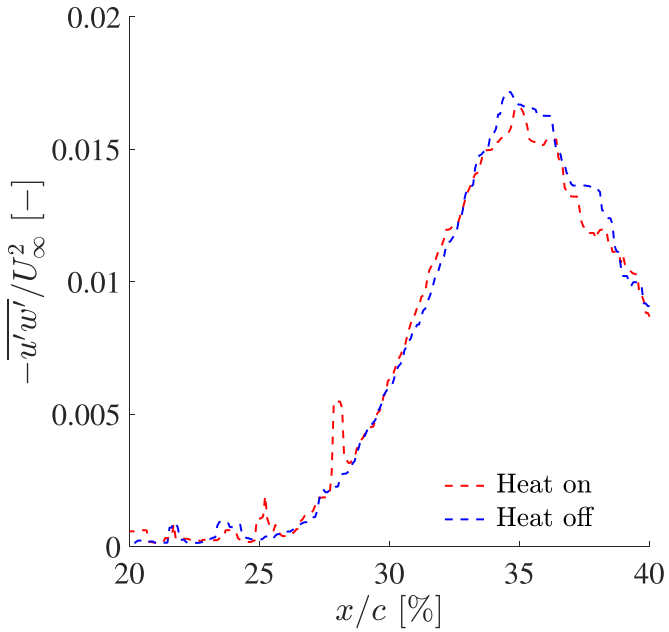

Figure 11. The maximum Reynolds shear stress along the wall-normal direction for the heat on and off cases.

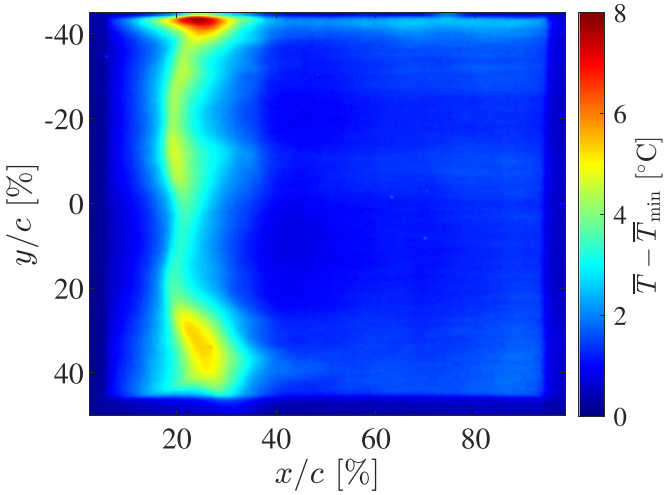

Figure 12. Time-averaged thermal field at a constant tow speed.

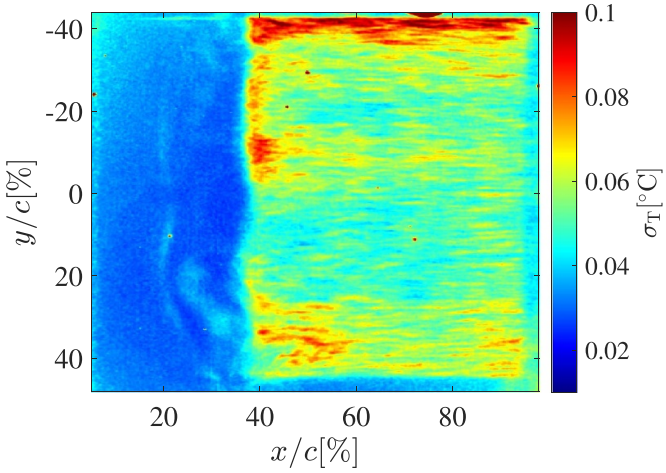

Figure 13. Standard deviation field of the thermal signal.

results (Guerra *et al* 2023). In the present study, the heat transfer based method suggested by Wynnychuk and Yarusevych (2020) is also considered. The normalized convective heat transfer coefficient can be computed as follows:

$$h^* = \frac{h}{h_{\text{free}}} \approx \frac{\overline{T_{\text{free}}} - T_{\text{free min}}}{\overline{T} - T_{\min}}. \tag{3}$$

In the present study, this quantity can only be approximated since the heat flux intensities employed at quiescent conditions in air with the horizontally placed foil and during the tow test with the vertically mounted foil are not equal.

Figure 14 displays the time-averaged temperature and h^* averaged over the span of the heating element ($-35\% \leqslant y/c \leqslant 40\%$), and the gradient of the physical quantities in the chordwise direction. x_S, x_T and x_R can be determined from the temperature based procedure at the local maximum and minimum of the streamwise gradient and at the local minimum of the surface temperature downstream of separation,

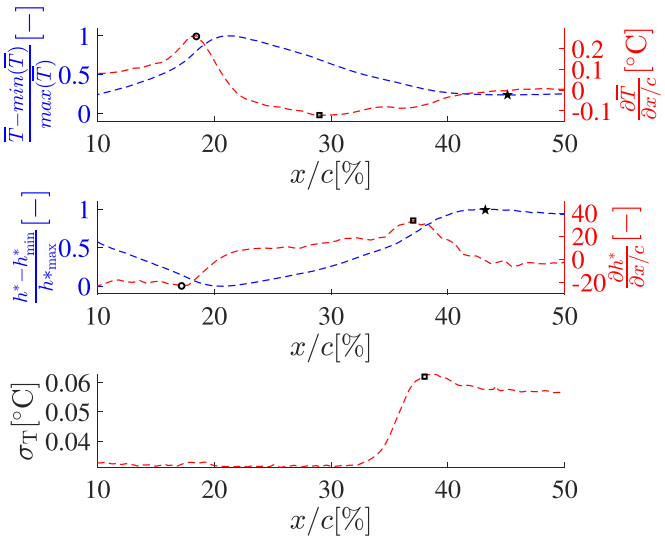

Figure 14. Time and spanwise averaged thermal field, normalized heat transfer distribution, and their gradient and the spanwise averaged standard deviation across the length of the foil. The black circle (○), square (□) and star (⋆) can be used to locate x_S, x_T and x_R, respectively.

Table 3. Time-averaged LSB locations on SD7003 foils.

Method/Source	x_S/c [%]	x_T/c [%]	x_R/c [%]
$\overline{T}$ and $\partial\overline{T}/\partial x$	18.4 ± 1.71	29.2 ± 3.67	45.1 ± 2.28
$\overline{h^*}$ and $\partial\overline{h^*}/\partial x$	17.2 ± 1.08	37.0 ± 1.44	43.2 ± 3.72
$\sigma_{T\ max}$		38.0 ± 1.23	
PIV.Heated.	15.2 ± 1.33		
PIV.Unheated.	16.1 ± 1.36		
(Burgmann and Schröder 2008) $Re_c = 6 \cdot 10^6$	20	28.5	31.5
(Burgmann and Schröder 2008) $Re_c = 4 \cdot 10^6$	19	33.0	36
(Nati *et al* 2015) $Re_c = 3 \cdot 10^6$	14	31.0	72
(Olson *et al* 2013) $Re_c = 4.6 \cdot 10^6$	17.5		53

respectively. Based on the normalized convective heat transfer coefficient estimate (h^*), the x_S, x_T and x_R lie at the minimum and maximum h^* coefficient gradient and at the local maximum of the heat transfer. Finally, the time-averaged transition location is also estimated based on the location of maximum root mean square surface temperature fluctuations (σ_T). The results are summarized in table 3. The temperature and pseudo heat transfer coefficient-based methods provide comparable estimates for the separation and reattachment location, with the former agreeing with PIV estimates to within the experimental uncertainty. However, a notable difference is seen between the estimates for the transition location. Here, the estimates from the pseudo heat transfer coefficient and temperature fluctuations methods fall within experimental uncertainty, while the prediction obtained based on temperature distributions deviates. In fact, the latter predicts transition closer to the separation than to the reattachment location, opposite to what is expected from the well established LSB topology (e.g. Burgmann and Schröder 2008, Hain *et al* 2009, Istvan and Yarusevych 2018). Acquiring the thermal field at quiescent conditions has thus proven to be essential to counteract the effects of local heat flux and heat transfer inhomogeneities. The characteristic locations of the LSB are in good general agreement with those reported in Burgmann and Schröder (2008), Nati *et al* (2015)and Olson *et al* (2013). The separation location has proven to be more invariant with the Re_c than the free-stream turbulence level. This explains the discrepancy between the location of the LSB in the present study and in the literature at approximately the same α. For example, compared to the LSB of Burgmann and Schröder (2008) at identical Re_c and α, the separation in the present study occurs farther upstream and the reattachment farther downstream, since the inflow turbulence level is lower in the present investigation.

3.3. The identification and characteristics of shear layer vortices

In this subsection, the ability of the experimental procedure to capture the propagation of shear layer roll-up vortices is evaluated. First, spectral analysis of the surface temperature measurements is considered. The spectral content is computed using Welch's method (Welch 1967). The number of samples per window in this case is 2^{11} with 50% overlap between temporal windows. The signal is extracted in the vicinity of the time-averaged transition location. The low disturbance environment in the towing tank should lead to the formation of spanwise coherent Kelvin–Helmholtz vortices (Istvan and Yarusevych 2018). The thermal signal can thus be averaged over the span of the heating element to reduce the noise level for the purposes of spectral analysis. Another commonly applied method is the averaging of the spectra computed at the same streamwise location across the span (Miozzi *et al* 2019). The results are displayed in figure 15. The spectra from the two methods reveal the dominant spectral peak at 4.4 ± 0.31 Hz, and secondary peaks at 6.3 ± 0.31 Hz and 8.4 ± 0.31 Hz. However, there is notable smoothing achieved by the spanwise averaging of the thermal signal. This approach may thus be beneficial for identifying the dominant fluctuations in the spectra of spanwise coherent structures. The wall-normal velocity fluctuations are also extracted at $x/c = 39\%$ and used to compute the power spectral density estimate. The data of every run is divided in temporal windows of 80 samples with 50% overlap between them and the resulting spectra are averaged over the 10 runs. The spectral content has shown no dependency on the heating and is displayed in figure 16 for the unheated case. The most amplified perturbation frequency is at 5.2 ± 0.15 Hz and secondary less amplified fluctuations are visible at 10.2 ± 0.15 Hz and 15.3 ± 0.15 Hz. The differences

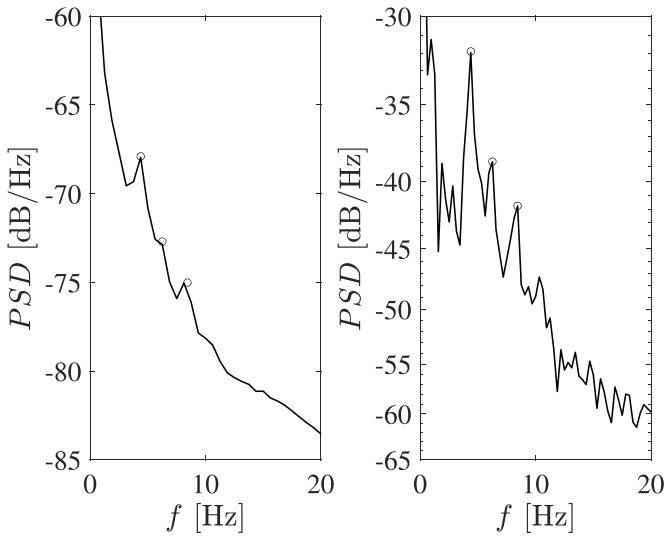

Figure 15. Left: average of the spectra computed along the span of the heating element and at $x/c = 39\%$. Right: spectrum of the spanwise averaged thermal signal extracted at $x/c = 39\%$. The high amplitude frequencies associated with spanwise coherent footprints are marked with circles.

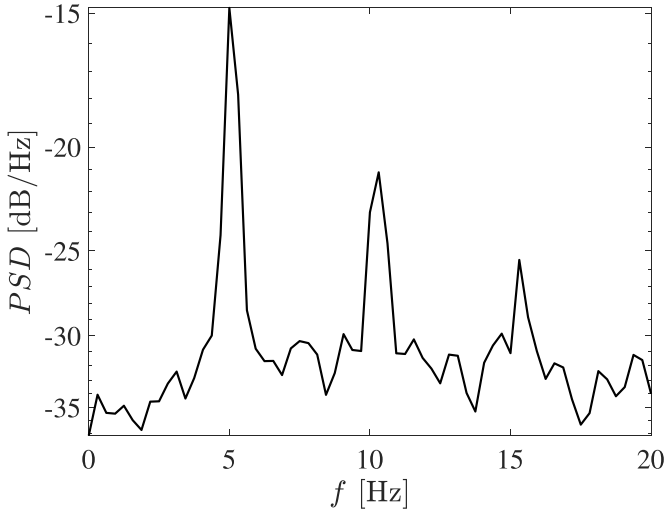

Figure 16. Spectral content in the vicinity of the time-averaged reattachment location ($x/c = 39\%$) derived from the wall-normal velocity fluctuations of the unheated case and extracted at the wall-normal location of the highest measured fluctuation amplitude.

in the spectra may have arisen from the different weight placed on the towing mechanism during the PIV and TSP measurements. Nonetheless, the estimate of most amplified frequency provided by the temperature based procedure coincides well with the PIV results.

A spectral proper orthogonal decomposition (Towne *et al* 2018) applied to the TSP data reveals spatial modes in figure 17 associated with dominant frequencies observed in the spectra displayed in figure 15. The results reveal spanwise-coherent footprints, with the earliest detectable traces occuring at approximately $x/c = 30\%$, which is slightly upstream of the time-averaged transition location. This is in agreement with the results of Kirk and Yarusevych (2017), who showed that the roll-up location in the free-shear layer is located upstream of the transition location. Near reattachment ($x/c \approx 42\%$), the spanwise coherence of the modes decays significantly, which indicates the roll-up vortices have deformed due to secondary instabilities and broken down into small scale structures, agreeing with the observations of Kurelek *et al* (2016).

3.4. The intermittent footprints

Apart from the footprints of the Kelvin–Helmholtz vortices, additional irregular V-shaped footprints were observed emerging between the transition and the reattachment location. An example is provided in figure 18, where a sequence of three instanteneous snapshots is presented. The revealed structures are nearly static spanwise oriented arcs originating near the reattachment location from which two legs emerge and extend downstream past the reattachment location. The origin of the V-shaped footprints is at approximately the same chordwise location and they appear to emerge in cascades. The upper- and lowermost footprints at approximately $y/c \approx -8\%$ and $y/c \approx 24\%$ are already visible in the first snapshot. The footprint at $y/c \approx 2.5\%$ appears in the second snapshot, and the tips of its legs are at approximately the same streamwise location as the leg tips of upper V-shaped footprint. The streamwise length of the middle footprint in the second snapshot is approximately $\Delta x/c = 6.1\%$ and it appeared in less than 0.04 convective time units, or within approximately 21% of the shear layer shedding period. This may indicate that the observed structures are related to the shear layer shedding, and their emergence may be linked to the advection of the associated shear layer structures towards the surface. The entrainment of cooler fluid from the outer flow then results in the observed lower surface temperature footprints. In the second frame, a faint spanwise coherent high temperature front can be observed slightly upstream of the connective arc of the V-shaped footprints. The same high temperature spanwise oriented front becomes more obvious at the third snapshot and is likely linked to the passage of the shear layer vortices. This may indicate that the vortical structures responsible for the V-shaped footprints occur in the braid region between the Kelvin–Helmholtz vortices. No additional thermal patterns can be observed between the arched structures and the connective arc always points towards the leading edge of the foil. Furthermore, no snapshot in which the legs of a footprint were connected to the ones of an adjacent one could be observed. It should be noted that the observed V-shaped footprints could not be observed outside of the heated region or in the reference images acquired with the static foil in the tank (see figure 19).

Predominantly streamwise oriented footprints, which could be observed in the study of Miozzi *et al* (2019) as well, can be observed downstream of x_R. These however do not depict a connective spanwise oriented arc.

The studies of Bernal and Roshko (1986) and Breidenthal (1981) focused on the secondary instabilities that occur in free-shear layers between subsequent Kelvin–Helmholtz vortices. Their respective flow visualization methods depicted a vortex filament connecting roll-up vortices through the braid region. Furthermore, in the direct numerical simulations of LSBs of

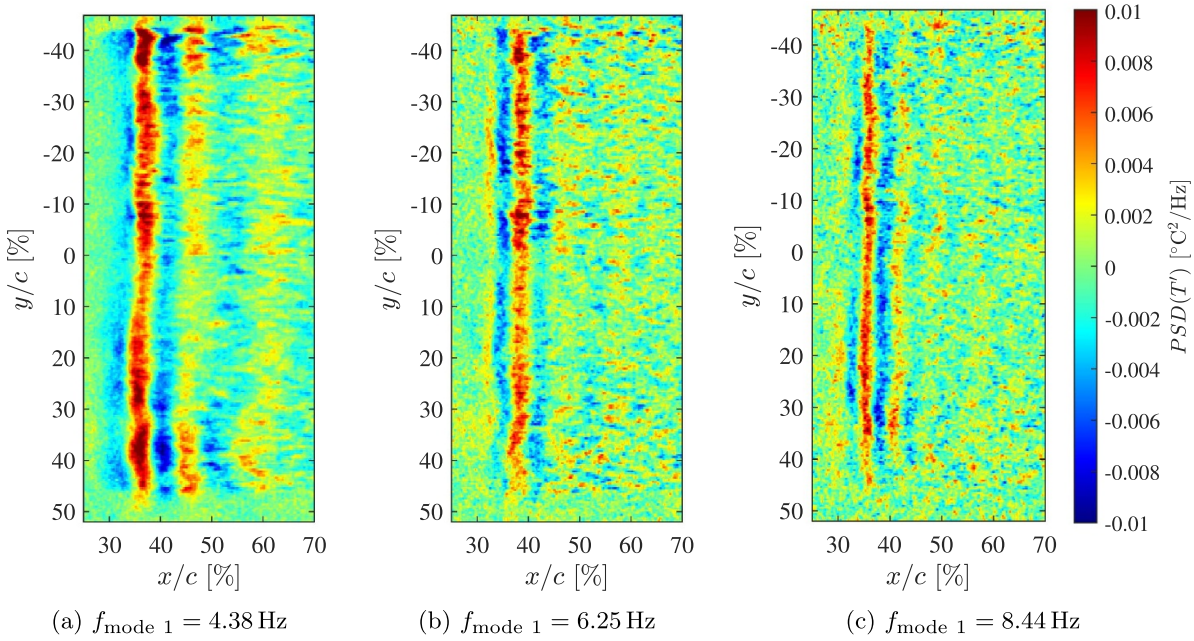

Figure 17. First SPOD mode spatial reconstruction at different relevant frequencies.

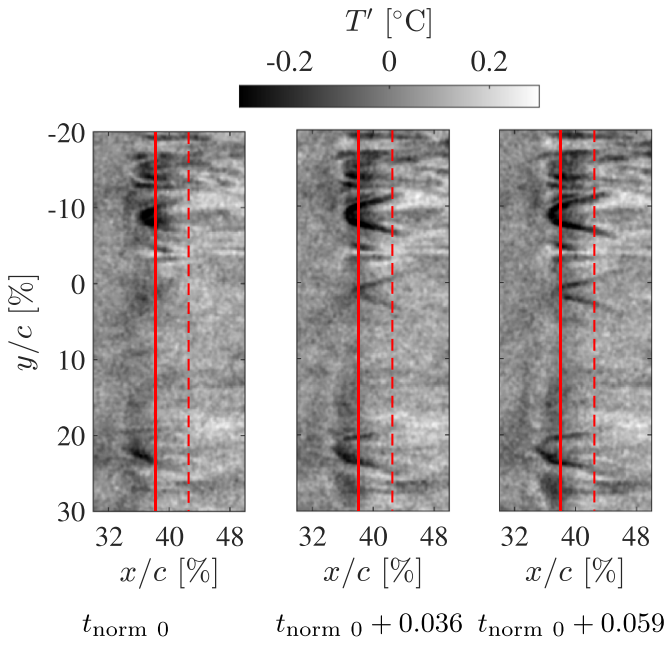

Figure 18. Thermal fluctuations snapshots at different normalized time entires. The continuous and dashed red lines represent the transition and reattachment locations, respectively.

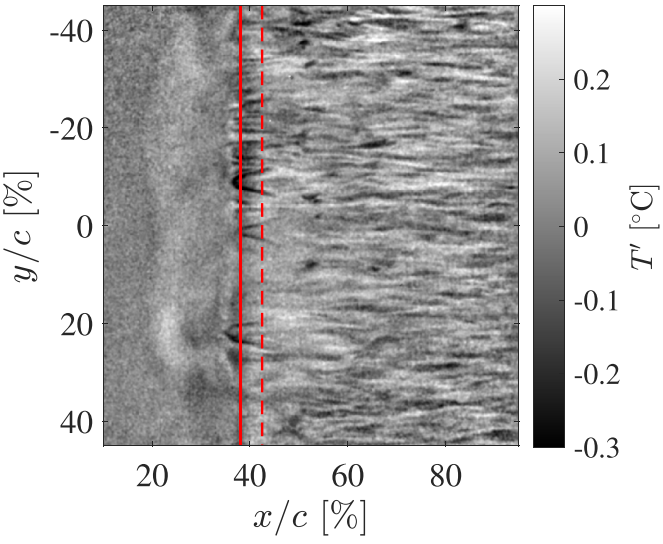

Figure 19. Wide field of view of the snapshot displayed at $t_{\text{norm 0}} + 0.059$ in figure 18. The continuous and dashed red lines represent the transition and reattachment locations, respectively.

Jones *et al* (2008) and Marxen *et al* (2013), streamwise oriented vorticity clusters of opposite signs were captured in the braid region at relatively low inflow turbulence levels. While they did not display a spanwise oriented connective vorticity arc contour similar to that observed in the present results (figure 18), the data were visualized by streamwise and spanwise vorticity contours at different planes. This supports the earlier conjecture that the observed V-shaped thermal footprints are related to secondary instabilities in the braid regions connecting shear layer vortices. We note that vortex breakdown is accelerated significantly at higher free-stream turbulence intensities (e.g. Istvan and Yarusevych 2018). This may be a reason why similar structures were not observed in the vicinity of reattachment in the study of Miozzi *et al* (2019), conducted at 0.6% free-stream turbulence intensity.

4. Summary

The purpose of this study was to develop an experimental procedure that can be used to analyse LSB dynamics based on TSP measurements. The europium based TSP, developed to

possess advantageous lifetime properties, provided the necessary light emission with reasonable illumination requirements. The single-shot lifetime method has been successfully implemented for the first time to resolve the highly unstable flow in the aft portion of LSBs. The necessary heating power for the experiments could furthermore be kept at a level which is sufficiently low to not significantly alter the base flow. This was confirmed by 2D2C PIV measurements. The methodology was applied to characterise an LSB forming on an SD7003 foil at $Re_c = 6 \cdot 10^4$ and an angle of attack of 6°.

The spraying technique of the heating layer caused variations in the distribution of the electrical resistance, which led to heat flux inhomogeneities. This issue was successfully mitigated by utilising measurements in quiescent conditions for the analysis of time-averaged LSB position. In particular, the analysis showed that the estimates of transition location directly from time-averaged temperature data were sensitive to heat flux inhomogeneities, while estimates of the separation and reattachment location were robust to the same. Employing either normalized heat transfer rate or σ_T of measured surface temperature fluctuations has been showed to provide reliable transition location estimates. The technique has thus been demonstrated to capture time-average locations of LSB, showing good agreement with PIV measurements and data from other studies.

The footprints of shear layer rollers occurring within the expected frequency range have been successfully identified by the employed procedure at $Re_c = 6 \cdot 10^4$ and an angle of attack of 6°. The technique has also been shown to capture the dynamics of shear layer vortices. Specifically, the footprints of shear layer rollers occurring within the expected frequency range have been successfully identified. The footprints show that shear layer vortices initially possess a relatively high level of spanwise coherence. The employed methodology has thus been demonstrated to provide insight into salient LSB characteristics and the dynamics of dominant coherent structures.

The study has demonstrated that the single-shot lifetime method is viable for detecting and quantifying time-resolved flow features. The use of this method can effectively mitigate the illumination instabilities occurring in the towing tank with a relatively low resource investment. Such advancements in the field of optical measurement methods provides access to information from the near wall region with high levels of detail with just one camera.

Data availability statement

All data that support the findings of this study are included within the article (and any supplementary files).

Acknowledgment

This work has been supported by the Deutsche Forschungsgemeinschaft (DFG, German Research Foundation), Grant Number 405970257. The authors would like to thank Carsten Fuchs (DLR) for the surface preparation, Daniel Droessler (DLR) for the surface quality measurements and Dr Marco Costantini (DLR) for the surface roughness measurements, as well as Dr Massimo Miozzi (CNR-INM), Dipl.-Ing. Wolfgang Dierl (University of the Bundeswehr Munich) and again Dr Marco Costantini (DLR) for the insightful conversations and constructive criticism.

ORCID iDs

Tudor V Venenciuc https://orcid.org/0009-0009-9081-6284
Christian Klein https://orcid.org/0000-0001-7592-6922

References

Abramov A and Butkovskii A 2021 Reynolds analogy for the fluid flow past a flat plate at different regimes *Phys. Fluids* **33** 017101
Bernal L and Roshko A 1986 Streamwise vortex structure in plane mixing layers *J. Fluid Mech.* **170** 499–525
Bitter M, Hara T and Hain R 2012 Characterization of pressure dynamics in an axisymmetric separating/reattaching flow using fast-responding pressure-sensitive paint *Exp. Fluids* **53** 1737–49
Bitter M and Kähler C 2011 Optische Bestimmung von OberfläChendruck- & Temperaturverteilungen am Naca Profil im Unter- und Transsschal *16 Fachtagung'Lasermethoden in der StröMungsmesstechnik* (Ilmenau, Germany) pp 6–8
Boyko A, Dovgal A and Kozlov V 1989 Nonlinear interactions between perturbations in transition to turbulence in the zone of laminar boundary-layer separation *Sov. J. Appl. Phys.* **3** 2
Breidenthal R 1981 Structure in turbulent mixing layers and wakes wing a chemical reaction *J. Fluid Mech.* **109** 1–24
Burgmann S and Schröder W 2008 Investigation of the vortex induced unsteadiness of a separation bubble via time-resolved and scanning piv measurements *Exp. Fluids* **45** 675–91
Capone A, Klein C and Di Felice F 2015 Fast-response underwater tsp investigation of subcritical instabilities of a cylinder in crossflow *Exp. Fluids* **56** 196
Costanini M, Fuchs C and Henne U 2021a Experimental analysis of the performance of a wind-turbine airfoil using temperature-sensitive paint *AIAA J.* **59** 11
Costanini M, Henne U and Klein K 2021b Skin-friction-based identification of the critical lines in a transonic, high reynolds number flow via temperature-sensitive paint *Sensors* **21** 5106
Dierl W, Hain R and Kähler C 2023 The Formation Process of a Laminar Separation Bubble Over an Sd7003 Airfoil at Various Accelerations (*30 Fachtagung'Experimentelle StröMungsmechanik) (Munich, Germany)* pp 5–7
Duan Z and He B 2014 Extended reynolds analogy for slip and transition flow heat transfer in microchannels and nanochannels *Int. Commun. Heat Mass Transfer* **56** 25–30
Filter S-G 2011 What is a Savitzky-Golay filter? IEEE Signal Processing Magazine (https://inst.eecs.berkeley.edu/ee123/sp18/docs/SGFilter.pdf) (Accessed 21 July 2022)
Gad-el H M 2001 Micro-air-vehicles: can they be controlled better? *J. Aircr.* **38** 3
Ghiaasiaan S (ed) 2011 *Convective Heat and Mass Transfer* (Cambridge University Press)
Goodman K, Lipford W and Watkins A 2016 Boundary-layer detection at cryogenic conditions using temperature sensitive paint coupled with a carbon nanotube heating layer *Sensors* **16** 2062
Guerra A, Mertens C and Little S 2023 Experimental characterization of an unsteady laminar separation bubble on a pitching wing *Exp. Fluids* **64** 16

Hain R, Kähler C and Radespiel R 2009 Dynamics of laminar separation bubbles at low-reynolds-number aerofoils *J. Fluid Mech.* **630** 129–53
Herbst S, Kähler C and Hain R 2020 Low aspect ratio wing under large-scale turbulent inflow conditions at low reynolds numbers (https://doi.org/10.1007/978-3-030-25253-3 62)
Hosseinverdi S and Fasel H 2018 Role of klebanoff modes in active flow control of separation: direct numerical simulations *J. Fluid Mech.* **850** 954–83
Istvan M and Yarusevych S 2018 Effects of free-stream turbulence intensity on transition in a laminar separation bubble formed over an airfoil *Exp. Fluids* **59** 52
Jones L, Sandberg R and Sandham N 2008 Direct numerical simulations of forced and unforced separation bubbles on an airfoil at incidence *J. Fluid Mech.* **602** 175–207
Kirk T and Yarusevych S 2017 Vortex shedding within laminar separation bubbles forming over an airfoil *Exp. Fluids* **58** 43
Klein C, Henne U and Sachs W 2014 Application of carbon nanotubes (CNT) and temperature-sensitive paint (TSP) for the detection of boundary layer transition *52nd Aerospace Sciences Meeting* (National Harbor) pp 13–17
Kurelek J, Lambert A and Yarusevych S 2016 Coherent structures in the transition process of a laminar separation bubble *AIAA J.* **54** 1–36
Kuwata Y 2021 Direct numerical simulation of turbulent heat transfer on the reynolds analogy over irregular rough surfaces *Int. J. Heat Fluid Flow* **92** 108859
Lang M, Rist U and Wagner S 2004 Investigations on controlled transition development in a laminar separation bubble by means of LDA and PIV *Exp. Fluids* **36** 43–52
Lienhard J and Lienhard J (eds) 2019 *A Heat Transfer Textbook* (Phlogiston Press)
Liu T, Sullivan J and Asai K (eds) 2021 *Pressure and Temperature Sensitive Paints* 2nd edn (Experimental Fluid Mechanics)
Liu T and Woodiga S 2011 Feasibility of global skin friction diagnostics using temperature sensitive paint *Meas. Sci. Technol.* **22** 11
Marxen O, Lang M and Rist U 2013 Vortex formation and vortex breakup in a laminar separation bubble *J. Fluid Mech.* **728** 58–90
Mebarki Y 2016 Pressure-sensitive paint measurements on a moving store in the NRC 1.5 m blowdown wind tunnel *32nd AIAA Aerodynamic Measurement Technology and Ground Testing Conf.* pp 13–17
Michelis T, Kotsonis M and Yarusevych S 2018 Spanwise flow development within a laminar separation bubble under natural and forced transition *Exp. Thermal Fluid Sci.* **96** 169–79
Miozzi M, Capone A and Costantini M 2019 Skin friction and coherent structures within a laminar separation bubble *Exp. Fluids* **60** 13
Miozzi M, Capone A and Di Felice F 2016 Global and local skin friction diagnostics from tsp surface patterns on an underwater cylinder in crossflow *Phys. Fluids* **28** 124101
Nati A, de Kat R and Scarano F 2015 Dynamic pitching effect on a laminar separation bubble *Exp. Fluids* **56** 172
Ol M, McAuliffe B and Hanff E 2005 Comparison of laminar separation bubble measurements on a low Reynolds number airfoil in three facilities *35th AIAA Fluid Dynamics Conf. and Exhibit* pp 6–9
Olson D, Katz A and Naguib A 2013 On the challenges in experimental characterization of flow separation over airfoils at low reynolds number *Exp. Fluids* **54** 1470
Ondrus V, Meier R and Klein C 2015 Europium 1,3-di(thienyl)propane-1,3-diones with outstanding properties for temperature sensing *Sensors and Actuators* A **233** 434–41
Raffel M, Willert C and Scarano F (eds) 2018 *Particle Image Velocimetry - A Practical Guide* 3rd edn) (Springer)
Rist U 2003 On instabilities and transition in laminar separation bubbles *Low ReynoldsNumber Aerodynamics on Aircraft Including Applications in Emerging* (UAV Technology)
Schlichting H and Gersten K 2017 *Boundary-Layer Theory* 9th edn (Springer)
Smith S and Brady J 1997 Susan-a new approach to low level image processing *Int. J. Comput. Vis.* **23** 45–78
Spalart P and Strelets M 2000 Mechanisms of transition and heat transfer in a separation bubble *J. Fluid Mech.* **403** 329–49
Thermoheld 2022 (available at: https://www.thermoheld.global) (Accessed 21 July 2022)
Towne A, Schmidt O and Colonius T 2018 Spectral proper orthogonal decomposition and its relationship to dynamic mode decomposition and resolvent analysis *J. Fluid Mech.* **847** 821–67
von Hoesslin S and Gruendmayer J 2019 Accessing quantitative heat transfer with temperature decline thermography *Exp. Thermal Fluid Sci.* **108** 55–60
Weiss A, Geisler R and Schwermer T 2017 Single-shot pressure-sensitive paint lifetime measurements on fast rotating blades using an optimized double-shutter technique *Exp. Fluids* **58** 120
Welch P 1967 The use of fast fourier transform for the estimation of power spectra: a method based on time averaging over short, modified periodograms *IEEE Trans. Audio Electroacustics* **AU- 15** 70–73
Wu J, Bitter M and Cai G 2017 Investigation on aerodynamic force effect of vacuum plumes using pressure-sensitive paint technique and CFD-DSMC solution *Sci. China Phys. Mech. Astron.* **60** 1058–67
Wynnychuk D and Yarusevych S 2020 Characterization of laminar separation bubbles using infrared thermography *AIAA Journal 58.* 2831–2843
Yarusevych S, Sullivan P and Kawall J 2009 On vortex shedding from an airfoil in low-reynolds-number flows *J. Fluid Mech.* **632** 245–71
Zhang W, Hain R and Kähler C 2008 Scanning PIV investigation of the laminar separation bubble on a SD7003 airfoil (available at: https://doi.org/10.1007/s00348-008-0563-8)